arXiv:1608.00348v1 [cond-mat.mes-hall] 1 Aug 2016

Enhanced thermoelectric performance in thin films of three-dimensional topological insulators

T. H. Wang and H. T. Jeng*

Department of Physics, National Tsing Hua University,

101 Section 2 Kuang Fu Road, Hsinchu,Taiwan 30013,R.O.C.

(Dated: August 2, 2016)

Abstract

Thermoelectric (TE) devices have been attracting increasing attention because of their ability to convert heat directly to electricity. To date, improving the TE figure of merit remains the key challenge. The advent of the topological insulator and the emerging nanotechnology open a new way to design high-performance TE devices. In this paper, we investigate the TE transport properties of the Bi_2Se_3 thin film by the first-principle calculations and the Boltzmann transport theory. By comparing our calculations with the earlier experimental data, we demonstrate that, for the Bi_2Se_3 film of thickness larger than six quintuple layers, the relaxation time of the topological surface states in the bulk gap is about hundreds of femtoseconds, which is about two orders larger than that of the bulk states. Such a large relaxation-time difference causes the ratio of the electrical conductance to the thermal conductance much larger than the value predicted by the Wiedemann-Franz law, as well as the large magnitude of Seebeck coefficient, and consequently the large TE figure of merit, when the Fermi level is near the conduction band edge. We shows that the TE performance can be further improved by introducing defects in the middle layers of the thin film. The improvement is generally significant at room temperature and can be further enhanced at higher temperature.

I. INTRODUCTION

Today, people faces numerous problems relating to energy supply and consumption. Nearly 70% of the world energy are wasted and dissipated into the environments as low grade heat[1]. Therefore, the thermoelectric (TE) generators, which can convert heat into electricity, having advantages of solid-state operation without moving parts, no release of greenhouse gases, good stability, and high reliability have attracted widespread research interest[2–9] However, the TE devices available to date are still in the limited application mainly because of its low energy-conversion efficiency.

Topological insulators (TIs), recently attracting great interest, are materials with an inverted bulk gap induced by the strong spin-orbit coupling and the metallic topological surface states (TSSs), which are protected by time reversal symmetry[10–16]. Most TIs such as Bi_2Te_3, Sb_2Te_3, and Bi_2Te_2Se are also good TE materials because the TIs and the TE materials generally share two common features, which are not directly related to the TSSs[17–21]. 1. The corrugated constant-energy surfaces and the complex band structures, generally can be caused by the band inversion in TIs, will lead to a high power factor in TE materials. 2. The large atomic mass, causing the strong spin-orbit coupling generally necessary to TIs, will bring about a low lattice thermal conductivity, which is beneficial to the TE performance. When the size is reduced to the nanometer scale, the TSSs will significantly change the TE performance for both the two-dimensional (2D) and the three-dimensional (3D) TIs[22,23]. Layered bismuth selenide (Bi_2Se_3) is one of the most intensively studied 3D TIs. It has a considerable bulk gap (~ 0.3 eV) and topologically protected metallic surface states[17,24,25]. Although the bulk crystalline Bi_2Se_3 is not a good TE material, it has been shown that the TE performance can be greatly enhanced by fabricating a single-layer-based composite made from atomically thick layers[26].

In this paper, we systematically study the TE performance of the Bi_2Se_3 thin film through the first-principle calculations and the Boltzmann transport theory. We mainly focus on the case of the film thickness larger than six quintuple layers (QLs) so that, as discussed later, the relaxation time of the TSSs in the bulk gap is about two orders of magnitude larger than that of the bulk states. Therefore, we will call the TSSs in the bulk gap the long lifetime states (LLSs) and the other states the short lifetime states (SLSs). We will explicate the effect of the large relaxation ratio between the LLSs and the SLSs on the TE parameters, and how it

improves the TE performance. The TE performance will be further improved when the SLS relaxation time τ_{SLS} is shorten without changing the LLS relaxation time τ_{LLS}. This can be achieved by introducing defects in the middle layers as discussed later. Unlike the common cases of small-gap materials, in which the bipolar effect can significantly deteriorates the TE performance at high temperature, such improvement of the TE performance is significant at room temperature and further enhanced at higher temperature. Although we only consider the case of Bi_2Se_3 thin film, similar enhancement of the TE performance is expected in some of the other 3D TI thin films.

II. METHOD

A. Electronic Structure

The electronic structure is calculated through the projector augmented wave (PAW) approach within the framework of density functional theory (DFT) as implemented in the Vienna Ab initio Simulation Package (VASP)[27–29]. The exchange-correlation is described in the Perdew-Burke-Ernzerhof (PBE) form of generalized gradient approximation (GGA)[30,31]. The spin-orbit coupling is taken into account. The $13 \times 13 \times 1$ Monkhorst–Pack mesh is used for k-point sampling within the Brillouin zone. The cutoff energy for plane wave basis is set as 450 eV. The energy convergence threshold is set to 10^{-9} eV in the self-consistent calculation. For structure relaxation, the van der Waals interactions between two adjacent quintuple layers are included using the DFT-D3 method with Becke-Jonson damping[32,33]. All the internal atomic coordinates and the lattice constant are relaxed until the magnitude of the force acting on all atoms is less than 0.5 meV/Å.

B. Transport properties

The efficiency of TE devices is determined by the dimensionless figure of merit[2]. For the case that the applied field of the thin film is along the in-plane direction, it can be expressed as

$$zT = \frac{\sigma S^2 T}{\kappa} \tag{1}$$

where T is the absolute temperature, S the Seebeck coeficiant, σ the electrical sheet conductance, and κ the thermal sheet conductance, which is the sum of its electronic part κ_e and its lattice part κ_L. Except for the lattice thermal conductance κ_L, all the TE parameters can be obtained from the Boltzmann transport equation with the relaxation time approximation. They can be expressed as

$$\sigma = \frac{e^2}{\hbar} I_0, \tag{2}$$

$$S = -\frac{k_B}{e}\frac{I_1}{I_0}, \tag{3}$$

$$\kappa_e = \frac{k_B^2 T}{\hbar}\left(I_2 - \frac{I_1^2}{I_0}\right), \tag{4}$$

where e is the elementary charge, k_B the Boltzmann constant, $\hbar$ the reduced Planck constant. The I_n is a dimensionless integral which can be written as

$$I_n = \int d\varepsilon \left(-\frac{\partial f_0}{\partial \varepsilon}\right)(\varepsilon - \varepsilon_f)^n \, \Sigma, \tag{5}$$

where $f_0 = 1/\left[\exp\left(\varepsilon - \varepsilon_f\right) + 1\right]$ is the Fermi-Dirac distribution function, ε_f the reduced Fermi level, and E_f the Fermi level. The Σ is the dimensionless transport distribution function (TDF)[34], which can be expressed as

$$\Sigma = \frac{\hbar}{(2\pi)^2}\int d^2k \delta\left(E - E_{\mathbf{k}}\right) v_{\mathbf{k}}^2 \tau_{\mathbf{k}}, \tag{6}$$

where $E_{\mathbf{k}}$ is the electronic band structure obtained from the DFT calculations, $v_{\mathbf{k}}$ the group velocity in the direction of the applied field, and $\tau_{\mathbf{k}}$ the relaxation time.

The lattice thermal conductance κ_L can be obtained through Callaway's model. It can be expressed as[35,36]

$$\kappa_L = \frac{k_B d}{2\pi^2 v_s}\left(\frac{k_B T}{\hbar}\right)^3 \int_0^{T_D/\sqrt[3]{5}T} dy \tau_c \frac{y^4 e^y}{\left(e^y - 1\right)^2}, \tag{7}$$

where d is the film thickness, v_s the sound velocity, T_D the Debye temperature, y proportional to the phonon frequency ω the dimensionless parameter $y = \hbar\omega/k_B T$. The τ_c is the phonon scattering relaxation time, which can be written as

$$\tau_c^{-1} = \frac{v_s}{d} + A\omega^4 + B\omega^2 T \exp\left(-\frac{\Theta_D}{CT}\right), \tag{8}$$

where $A = 9.42 \times 10^{-42}$ (s^3), $B = 7.78 \times 10^{-18}$ (sK^{-1}) and $C = 2.8$ are parameters independent of temperature[36]. The three terms of equation (8) represent, respectively, the boundary scattering, the point defect (Rayleigh) scattering, and the phonon-phonon scattering.

III. RESULTS AND DISCUSSION

A. Electronic Structure & Electron Scattering

The electronic structure of the Bi_2Se_3 thin film of thickness 8 QLs is shown in Fig. 1b, in which we can see the massless Dirac cone with the Dirac point at zero energy. The Dirac-cone states are doubly degenerate states, which can be regarded as two TSSs on different sides of the film. As can be seen, there is a bulk gap, the energy region between the valence band edge (VBE) $E_v = -0.5$ meV and the conduction band edge (CBE) $E_c = 295$ meV indicated by the yellow shaded region, in which there is no electronic states except for the TSSs. The wave functions of the TSSs on different sides of the film are spatially separated so that the orbital contribution from the atoms in the middle 2 QLs (indicated by the red box in Fig. 1a) is less than 1%. The TSSs in the bulk gap (hereafter call the LLSs) should have long relaxation times due to two reasons. (i) The large-angle scattering between the TSSs on the same side of the thin film is suppressed because the spin polarization of the TSSs circulates around the Γ point as can be seen in Fig. 1c. (ii) The scattering between the TSSs on the opposite sides of the thin film is negligible because of the spatial separation between the initial and final states as mentioned above. The relaxation times of the other states (hereafter call the SLSs), τ_{SLS}, should be much smaller than that of the LLSs, τ_{LLS}, because the electrons of the SLSs can be elastically scattered into the bulk states. The long relaxation time of the TSSs in the bulk gap (i.e., the LLSs) can be demonstrated by comparing our computed value of the sheet conductance with the experimental data in ref. 37 (see Supplementary Information for more details). The estimated value is 230 fs, which is about two orders higher than that of bulk relaxation time ($\sim$ 2.7 fs)[38]. In this paper, we adopt the dual relaxation time model, which is a generalization of the conventional constant relaxation time approximation[22]. In this model, the relaxation times τ_{LLS} and τ_{SLS} are two constants. The integral I_n is divided into the LLS part I_n^{LLS} and the SLS part I_n^{SLS}. Then we can define the LLS (SLS) electrical conductance σ_{LLS} (σ_{SLS}), and the LLS (SLS) Seebeck coefficient S_{LLS} (S_{SLS}) by the equations the same as equations (2) and (3), except that the integral is replaced by the I_n^{LLS} (I_n^{SLS}). According to this definition, the electrical conductance is the sum of the LLS and the SLS conductances[39],

$$\sigma = \sigma_{LLS} + \sigma_{SLS}. \tag{9}$$

On the other hand, the Seebeck coefficient is a weighted average of the Seebeck coefficients associated with the two type of the carriers,

$$S = \frac{\sigma_{LLS} S_{LLS} + \sigma_{SLS} S_{SLS}}{\sigma_{LLS} + \sigma_{SLS}} \tag{10}$$

B. Thermoelectric transport properties

The room-temperature TE figure of merit of the 8QL Bi_2Se_3 film as a function of the Fermi level is shown in Fig. 2a. Here, the relaxation time of the LLSs and the SLSs are, respectively, set to be 230 fs and 1 fs. As can be seen, there are four zT peaks denoted by P1-P4, among which the P1 (P4) is located away from the VBE (CBE). When the Fermi level is near the P1 or P4 energy, the conduction carriers are almost the SLS carriers. On the other hand, the peak P2 (P3) is located near the VBE (CBE). When the Fermi level is around the P2 (P3) energy, both the LLSs and the SLSs are significant to the TE performance. The zT peak values of P2 and P3 are much greater than those of P1 and P4. Hereafter, we will mainly focus on P2 and P3. Sometimes, we may only discuss the case of P3, and the discussion of P2 is similar to that of P3 unless otherwise mentioned.

Figure 2b shows the electrical sheet conductance as a function of the Fermi level. As can be seen, when the Fermi level is located in the bulk gap, the magnitude of the total conductance is nearly equal to that of the LLS contribution. Because the LLS density of states (DOS) increases with the Fermi level, the conductance increases with the Fermi level to the maximum at the energy about $2.5k_BT$ (or 65 meV) below the CBE. It then decreases because of the decline in the conduction carrier number of the LLSs regardless the increase in that of the SLSs. When the Fermi level is at the P3 energy, which is 42 meV above the CBE, the conduction carrier number of the SLSs is much larger than that of the LLSs. Nevertheless, the total conductance is mainly contributed from the LLS conductance σ_{LLS} because of the large relaxation time difference between the LLSs and the SLSs.

The Seebeck coefficient as a function of the Fermi level is shown in Fig. 2c. Similar to the typical semiconductor cases, the SLS Seebeck coefficient S_{SLS} is negative for n-type doping ($E_f \gtrsim E_c$) and positive for p-type doping ($E_f \lesssim E_v$). When the Fermi level is in the bulk gap and away from the midgap, the magnitude of the S_{SLS} increases as the Fermi level moves toward the midgap. This can be easily comprehended by rewriting the Seebeck

coefficients of the LLSs and the SLSs as

$$S_i = -\frac{\langle E \rangle_i - E_f}{eT}, \tag{11}$$

where

$$\langle E \rangle_i = \frac{\int_{\Delta_i} d\varepsilon \left(-\frac{\partial f_0}{\partial \varepsilon}\right) \Sigma E}{\int_{\Delta_i} d\varepsilon \left(-\frac{\partial f_0}{\partial \varepsilon}\right) \Sigma} \tag{12}$$

is the TDF-weighted average energy of the conduction carriers, and Δ_{LLS} (Δ_{SLS}) the energy region of the LLSs (SLSs), i.e. the yellow (white) shaded region in Figs. 1b and 2. For n-type (p-type) doping, almost all the conduction carriers and hence the $\langle E \rangle_{SLS}$ are slight higher (lower) than the CBE (VBE) so that the magnitude of the S_{SLS} increase as the Fermi level moves toward the midgap. Due to the bipolar effect, the magnitude of the S_{SLS} reduces near the middle of the gap[39]. The LLS Seebeck coefficient S_{LLS} generally has a sign opposite to the SLS Seebeck coefficient S_{SLS}. The magnitude of the LLS Seebeck coefficient increases as the Fermi level moves away from the energy region of the LLSs. This can also be comprehended from equation (11) by considering the fact that the $\langle E \rangle_{LLS}$ is located in the energy region Δ_{LLS}. The energy of $S_{LLS} = 0$ is higher than the midgap energy because the LLS DOS increases with energy. As defined in equation (10), the Seebeck coefficient is a conductance-weighted average of the LLS and the SLS Seebeck coefficients. In the limit $\tau_{SLS} \ll \tau_{LLS}$, the Seebeck coefficient is nearly equal to LLS Seebeck coefficients, whose magnitude is extraordinarily large when the Fermi level is away from the energy region Δ_{LLS}. In the present case, the relaxation time of the SLSs is indeed much smaller than that of the LLSs. The resultant magnitude of the Seebeck coefficient at P3 (P2) is nearly the same as magnitude of the S_{LLS} and it is as large as 0.21 (0.16) mV/K.

The ratio of the electrical conductance to the electronic thermal conductance σ/κ_e as a function of the Fermi level is shown in Fig. 2d. It is normalized in unit of $R_{WF} = 3e^2/\pi^2 k_B^2 T$, which is the value given by the Wiedemann-Franz law[40]. As can be seen, the Wiedemann-Franz law is generally applicable (i.e., $\sigma/\kappa_e \sim R_{WF}$) except for the energy around the band edges. The Wiedemann-Franz law can be derived by applying the Sommerfeld expansion on equation (5) and retaining the lowest non-vanishing order[40]. Because the relaxation time of the electrons near the band edge and the corresponding TDF vary rapidly with the energy, the higher-order terms are significant. By taking into account the higher-order terms and

replacing Σ with $\int d\varepsilon \left(-\frac{\partial f_0}{\partial \varepsilon}\right) \Sigma$, the ratio σ/κ_e can be approximated as

$$\frac{\sigma}{\kappa_e} \approx R_{WF} \left[1 + \frac{\pi^2}{3} \left(\frac{k_B T \sigma'}{\sigma}\right)^2 - \frac{8\pi^2}{15} \frac{(k_B T)^2 \sigma''}{\sigma}\right], \tag{13}$$

where the prime denotes the derivative with respect to E_f. The first term is just the result of the Wiedemann-Franz law. In the energy region slightly below the CBE, the electrical conductance decreases rapidly with energy. The second term becomes significant, and the ratio σ/κ_e increases with energy to a value much larger than R_{WF}. When the energy further increases, the dominant type of the conduction carriers changes from the LLS to the SLS and the sign of the σ' changes from negative to positive. This leads to the decrease of the magnitude of the σ' and a considerable positive σ''. As a result, the ratio σ/κ_e decreases with energy to a value smaller than R_{WF}. Because the magnitude of the Seebeck coefficient increases with energy, the peak P3 is always located at the energy region where the ratio σ/κ decreases with energy. The ratio σ/κ_e at P3 energy is more than twice larger than the value given by the Wiedemann-Franz law. Unlike the case of $E_f \sim E_c$, the ratio σ/κ_e shows no significant increase as $E_f \sim E_v$. This is mainly because the energy of the Dirac point is nearly the same as that of the VBE. The LLS DOS near the VBE is much smaller than that near the CBE. Therefore, the variation of the TDF with energy near the VBE is not as significant as that near the CBE. This is also the reason why the figure of merit at P2 is smaller than that at P3 and why the P2 is located in the energy region Δ_{LLS} while the P3 is in the Δ_{SLS}.

C. Further Enhancement by shortening the SLS relaxation time

The TE performance can be further enhanced by reducing the SLS relaxation time. This can be done without changing the LLS relaxation time by introducing defects in the middle layers as mentioned earlier. As an example, we calculate the TE parameters at temperature $T = 600$ K as shown in Fig. 3. Figure 3a-e shows the results of $\tau_{SLS} = 2$ fs and Fig. 3k-o the results of $\tau_{SLS} = 0.2$ fs. The TE parameters as functions of the SLS relaxation time in the range from 0.2 to 2 fs for $E_f = 0.34$ eV (the P3 energy for $\tau_{SLS} = 2$ fs) are shown in Fig. 3f-j. As can be seen in Fig. 3b and 3l, when the SLS relaxation time reduces from 2 fs to 0.2 fs, the SLS conductance becomes negligible around the P3 energy. This causes the increase (decrease) of the magnitude of σ' (σ''). The increase (decrease) of the magnitude

of σ' (σ'') leads to the increase of the ratio σ/κ_e as shown in Fig. 3i. Furthermore, the magnitude of the Seebeck coefficient increases with the decreasing SLS relaxation time. It is nearly equal to the magnitude of LLS Seebeck coefficient when $\tau_{SLS} = 0.2$ fs as shown in Fig. 3j. These cause the remarkable increase in the figure of merit at P3 energy from 1.31 to 2.94 (see Fig. 3f) in spite of the slight decrease of the electrical conductance (see Fig. 3g). The reduction of the SLS relaxation time results in the blue shift of the P3 energy as indicated by the blue and green dashed lines in Figs 3a, k. This further enhances the figure of merit to the value of $zT = 3.8$. In addition, we perform similar calculation for the room temperature (see Fig. S3). We find the figure of merit is also significantly enhanced. It increases from 1.67 to 2.77 when the SLS relaxation time decreases from 2 fs to 0.2 fs.

Figure 4 is a low-temperature ($T = 100$ K) counterpart of Fig. 3. As can be seen, the magnitude of the figure of merit only slightly increases from 0.90 to 1.06 when the SLS relaxation time reduces from 2 fs to 0.2 fs. In addition, it would be difficult to experimentally tune the Fermi level in such a narrow peak width (~ 0.02 eV) at low temperature as can be seen in Fig 3a, k. Unlike the high-temperature ($T = 600$ K) case, in which the electronic thermal conductance is generally much larger than the lattice thermal conductance as shown in Fig. 3c, h and m, the electronic thermal conductance at low temperature ($T = 100$ K) near the P3 energy is much smaller than the lattice thermal conductance as shown in Fig. 4c, h and m. Consequently, the ratio σ/κ is nearly a constant even though the ratio σ/κ_e increases significantly with the decrease of the SLS relaxation time as shown in Fig. 4i.

D. Thickness Dependence of the TE Performance

Figure 5a shows the figure of merit of the 7, 8 and 10QL Bi_2Se_3 thin films at room temperatue. As can be seen, the figure of merit of P2 and P3 decreases with the film thickness. Figure 5b is the same as Fig. 5a except that the lattice thermal conductance κ_L of the 7QL and the 9QL films is set at the value the same as that of the 8QL film. We find the figure of merit difference between the films of different thickness is greatly reduced indicating that the decrease of the figure of merit with increasing thickness is mainly due to the increase of the lattice thermal conductance. As we mentioned earlier, the TE performance can be enhanced by introducing defects into the middle layers of the thin film so that the SLS relaxation time can be reduced without changing the LLS relaxation time. For the case of

larger film thickness, the low SLS relaxation time should be more easily to achieve. However, the thermal conductance increases at the same time. As we discussed earlier, the figure of merit will barely increase with decreasing SLS relaxation time if the electronic thermal conductance κ_e is much smaller than the lattice thermal conductance κ_L. Therefore, the optimized film thickness should be the smallest thickness that the condition $\kappa_e \ll \kappa_L$ can be satisfied by introducing defects. In addition, it should not be smaller than 6 QLs as discussed below.

Thus far, we consider the case of the film thickness larger than 6 QLs. When the film thickness is smaller than 6 QLs, the LLS relaxation time will be dramatically reduced by the scattering between the TSSs on the opposite sides as demonstrated in Supplementary Information. In this case, introducing defects into the Bi_2Se_3 thin film will significantly reduce not only the SLS relaxation time τ_{SLS} but also the LLS relaxation time τ_{LLS}. Figure 5c shows the figure of merit of the 5QL Bi_2Se_3 thin film for the LLS relaxation times shorter than 230 fs in the case of the SLS relaxation time $\tau_{SLS} = 1$ fs at temperature $T = 600$. The corresponding zT maximum for n-type (p-type) doping as a function of the LLS relaxation time is shown in Fig. 5d. Here, the n-type (p-type) doping is defined as the maximum zT in the case of the Fermi level higher (lower) than 0.2 eV. As can be seen, the figure of merit generally decreases with decreasing LLS relaxation time. For n-type doping, the zT maximum reduces from 2.9 to 0.1 when the LLS relaxation time decreases from 230 fs to 12 fs. When the LLS relaxation is reduced to about 15 fs, the LLS conductance is comparable with the SLS conductance causing a strong cancelation between the LLS Seebeck coefficient and the SLS Seebeck coefficient as indicated by equation (10). The relatively small relaxation time ratio τ_{LLS}/τ_{SLS} also deteriorates the TE performance by reducing the ratio of σ/κ_e as indicated in equation (13). When the LLS relaxation time further decreases, the figure of merit at P4 (P1) is larger than that at P3 (P2). In this case, the zT maximum increases with decreasing τ_{LLS} because the bulk carriers dominate the transport when the Fermi level is at P4 (P1) energy. Finally, when the LLS relaxation time is reduced to 1 fs (i.e., $\tau_{LLS} = \tau_{SLS}$), the P2 and P3 disappear, and only the P1 and P4 remain. The quite large zT maximum for p-type doping is mainly due to the large DOS of the valence bands.

IV. CONCLUSIONS

In summary, we investigate the TE properties of the Bi_2Se_3 thin film through the first-principle calculations and the Boltzmann transport theory. When the film thinness is so large ($>$ 6 QLs) that the coupling between the TSSs on the opposite sides of the film is negligible, the large-angle scattering is strongly suppressed, and the relaxation time of the LLSs can be hundreds of times larger than that of the SLSs as demonstrated by comparing our calculations with the earlier experimental data (see Supplementary Information). As a result, the reduction of the magnitude of the Seebeck coefficient near the P3 (P2) energy caused by the SLS carriers is negligible and the Seebeck coefficient is nearly equal to the LLS Seebeck coefficient. The ratio of the electrical conductance to the electronic thermal conductance can be dramatically deviated from the value given by the Wiedemann-Franz law R_{WF} when the Fermi level is near the band edges and much larger than R_{WF} when the Fermi level is at the P3 energy. The TE performance can be further enhanced by reducing the SLS relaxation time without changing LLS relaxation time. This enhancement is prominent especially at high temperature and achievable by introducing defects in the middle layers. When the film thickness increases to 10 QLs, the figure of merit decreases mainly due to the increase of the thermal conductance. When the film thickness decreases to the thickness smaller than 6 QLs, the TE performance will be greatly deteriorated because of the effective coupling between the TSSs on the opposite sides of the thin film. The optimized film thickness would be the smallest one, that can satisfy the condition $\kappa_e \ll \kappa_L$ by introducing defect in the region more than 3 QLs away from the surface, and should be not smaller than 6 QLs. Although we only consider the thin films made of Bi_2Se_3, the high TE performance caused by the coexistence of the LLS and SLS conduction carriers is expected in some of the other TI thin films.

Acknowledgement 1 *This work was supported by the Ministry of Science and Technology, Taiwan.*

* Electronic address: jeng@phys.nthu.edu.tw

[1] Zevenhoven, R. & Beyene, A. The relative contribution of waste heat from power plants to global warming. *Energy* **36**, 3754-3762 (2011).

[2] Rowe, D. M. (ed.) CRC *Handbook of thermoelectrics*. (CRC Press, 1955).

[3] Tritt, T. M. & Subramanian, M. A. Thermoelectric materials, phenomena, and applications: A bird's eye view. *Mrs Bull* **31**, 188-194 (2006).

[4] Snyder, G. J. Small thermoelectric generators. *Electrochem. Soc. Interface* **17**, 54 (2008).

[5] Tritt, T. M. Thermoelectric phenomena, materials, and applications. *Annu. Rev. Mater. Res.* **41**, 433-448 (2011).

[6] Alam, H. & Ramakrishna, S. A review on the enhancement of figure of merit from bulk to nano-thermoelectric materials. *Nano Energy* **2**, 190-212 (2013).

[7] He, W., Zhang, G., Zhang, X. X., Ji, J., Li, G. Q. & Zhao, X. D. Recent development and application of thermoelectric generator and cooler. *Appl. Energ.* **143**, 1-25 (2015).

[8] Aswal, D. K., Basu, R. & Singh, A. Key issues in development of thermoelectric power generators: High figure-of-merit materials and their highly conducting interfaces with metallic interconnects. *Energ. Convers. Manage.* **114**, 50-67 (2016).

[9] Zhang, Q. H., Huang, X. Y., Bai, S. Q., Shi, X., Uher, C. & Chen, L. D. Thermoelectric devices for power generation: Recent progress and future challenges. *Adv. Eng. Mater.* **18**, 194-213 (2016).

[10] Kane, C. L. & Mele, E. J. Z(2) topological order and the quantum spin Hall effect. *Phys. Rev. Lett.* **95**, 146802 (2005).

[11] Bernevig, B. A. & Zhang, S. C. Quantum spin hall effect. *Phys. Rev. Lett.* **96**, 106802 (2006).

[12] Fu, L., Kane, C. L. & Mele, E. J. Topological insulators in three dimensions. *Phys. Rev. Lett.* **98**, 106803 (2007).

[13] Moore, J. E. & Balents, L. Topological invariants of time-reversal-invariant band structures. *Phys. Rev. B* **75**, 121306 (2007).

[14] Qi, X. L., Hughes, T. L. & Zhang, S. C. Topological field theory of time-reversal invariant insulators. *Phys. Rev. B* **78**, 195424 (2008).

[15] Hasan, M. Z. & Kane, C. L. Colloquium: Topological insulators. *Rev. Mod. Phys.* **82**, 3045-3067

(2010).

[16] Bansil, A., Lin, H. & Das, T. Colloquium: Topological band theory. *Rev. Mod. Phys.* **88** (2016).

[17] Zhang, H. J., Liu, C. X., Qi, X. L., Dai, X., Fang, Z. & Zhang, S. C. Topological insulators in Bi_2Se_3, Bi_2Te_3 and Sb_2Te_3 with a single Dirac cone on the surface. *Nat. Phys.* **5**, 438-442 (2009).

[18] Chen, Y. L., Analytis, J. G., Chu, J. H., Liu, Z. K., Mo, S. K., Qi, X. L., Zhang, H. J., Lu, D. H., Dai, X., Fang, Z., Zhang, S. C., Fisher, I. R., Hussain, Z. & Shen, Z. X. Experimental realization of a three-dimensional topological insulator, Bi_2Te_3. *Science* **325**, 178-181 (2009).

[19] Xie, W. J., He, J., Kang, H. J., Tang, X. F., Zhu, S., Laver, M., Wang, S. Y., Copley, J. R. D., Brown, C. M., Zhang, Q. J. & Tritt, T. M. Identifying the specific nanostructures responsible for the high thermoelectric performance of $(Bi,Sb)_2Te_3$ nanocomposites. *Nano Lett.* **10**, 3283-3289 (2010).

[20] Muchler, L., Casper, F., Yan, B. H., Chadov, S. & Felser, C. Topological insulators and thermoelectric materials. *Phys. Status Solidi-R* **7**, 91-100 (2013).

[21] Shi, H. L., Parker, D., Du, M. H. & Singh, D. J. Connecting thermoelectric performance and topological-insulator behavior: Bi_2Te_3 and Bi_2Te_2Se from first principles. *Phys. Rev. Appl.* **3** (2015).

[22] Xu, Y., Gan, Z. X. & Zhang, S. C. Enhanced thermoelectric performance and anomalous Seebeck effects in topological insulators. *Phys. Rev. Lett.* **112**, 226801 (2014).

[23] Liang, J. H., Cheng, L., Zhang, J., Liu, H. J. & Zhang, Z. Y. Maximizing the thermoelectric performance of topological insulator Bi_2Te_3 films in the few-quintuple layer regime. *Nanoscale* **8**, 8863-8870 (2016).

[24] Xia, Y., Qian, D., Hsieh, D., Wray, L., Pal, A., Lin, H., Bansil, A., Grauer, D., Hor, Y. S., Cava, R. J. & Hasan, M. Z. Observation of a large-gap topological-insulator class with a single Dirac cone on the surface. *Nat. Phys.* **5**, 398-402 (2009).

[25] Hsieh, D., Xia, Y., Qian, D., Wray, L., Dil, J. H., Meier, F., Osterwalder, J., Patthey, L., Checkelsky, J. G., Ong, N. P., Fedorov, A. V., Lin, H., Bansil, A., Grauer, D., Hor, Y. S., Cava, R. J. & Hasan, M. Z. A tunable topological insulator in the spin helical Dirac transport regime. *Nature* **460**, 1101-1105 (2009).

[26] Sun, Y. F., Cheng, H., Gao, S., Liu, Q. H., Sun, Z. H., Xiao, C., Wu, C. Z., Wei, S. P. & Xie, Y. Atomically thick bismuth selenide freestanding single layers achieving enhanced thermoelectric

energy harvesting. *J. Am. Chem. Soc.* **134**, 20294-20297 (2012).

[27] Kresse, G. & Furthmuller, J. Efficiency of ab-initio total energy calculations for metals and semiconductors using a plane-wave basis set. *Comp. Mater. Sci.* **6**, 15-50 (1996).

[28] Kresse, G. *Ab initio* molecular dynamics for liquid-metals. *J. Non-Cryst Solids* **193**, 222-229 (1995).

[29] Kresse, G. & Furthmuller, J. Efficient iterative schemes for *ab initio* total-energy calculations using a plane-wave basis set. *Phys. Rev. B* **54**, 11169-11186 (1996).

[30] Perdew, J. P., Chevary, J. A., Vosko, S. H., Jackson, K. A., Pederson, M. R., Singh, D. J. & Fiolhais, C. Atoms, molecules, solids, and surfaces: Applications of the generalized gradient approximation for exchange and correlation. *Phys. Rev. B* **46**, 6671-6687 (1992).

[31] Perdew, J. P. & Wang, Y. Pair-Distribution Function and Its Coupling-Constant Average for the Spin-Polarized Electron-Gas. *Phys. Rev. B* **46**, 12947-12954 (1992).

[32] Grimme, S., Antony, J., Ehrlich, S. & Krieg, H. A consistent and accurate ab initio parametrization of density functional dispersion correction (DFT-D) for the 94 elements H-Pu. *J. Chem. Phys.* **132** (2010).

[33] Grimme, S., Ehrlich, S. & Goerigk, L. Effect of the damping function in dispersion corrected density functional theory. *J. Comput. Chem.* **32**, 1456-1465 (2011).

[34] Mahan, G. D. & Sofo, J. O. The best thermoelectric. *Proc. Natl. Acad. Sci. USA* **93**, 7436-7439 (1996).

[35] Callaway, J. Model for lattice thermal conductivity at low temperatures. *Phys. Rev.* **113**, 1046-1051 (1959).

[36] Navratil, J., Horak, J., Plechacek, T., Kamba, S., Lost'ak, P., Dyck, J. S., Chen, W. & Uher, C. Conduction band splitting and transport properties of Bi_2Se_3. *J. Solid State Chem.* **177**, 1704-1712 (2004).

[37] Taskin, A. A., Sasaki, S., Segawa, K. & Ando, Y. Manifestation of topological protection in transport properties of epitaxial Bi_2Se_3 thin films. *Phys. Rev. Lett.* **109**, 066803 (2012).

[38] Luo, X., Sullivan, M. B. & Quek, S. Y. First-principles investigations of the atomic, electronic, and thermoelectric properties of equilibrium and strained Bi_2Se_3 and Bi_2Te_3 including van der Waals interactions. *Phys. Rev. B* 86, 184111 (2012).

[39] Goldsmid, H. J. *Introduction to thermoelectricity*. Vol. 121 (Springer, 2009).

[40] Aschcroft, N. W. & Mermin, N. D. *Solid state physics*. (Holt-Saunders, 1976).

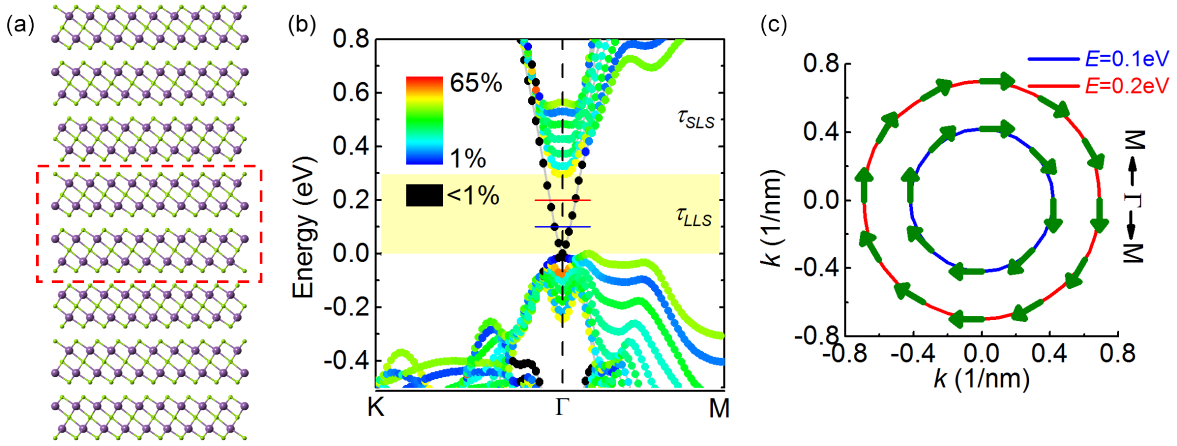

FIG. 1: **The crystal structure and the electronic band structure of the** 8**QL** $\mathbf{Bi_2Se_3}$**.** (**a**) The crystal structure. (**b**) The electronic band structure. The yellow shaded region denotes of energy region of the LLSs, which is also the bulk gap. The color of the data points represents the orbital contribution from the atoms in the middle 2 QLs indicated by the red box in (**a**). When it is black, the orbital contribution from the atoms in the middle 2 QLs is less than 1%. (**c**) The spin texture of the constant energy contours.

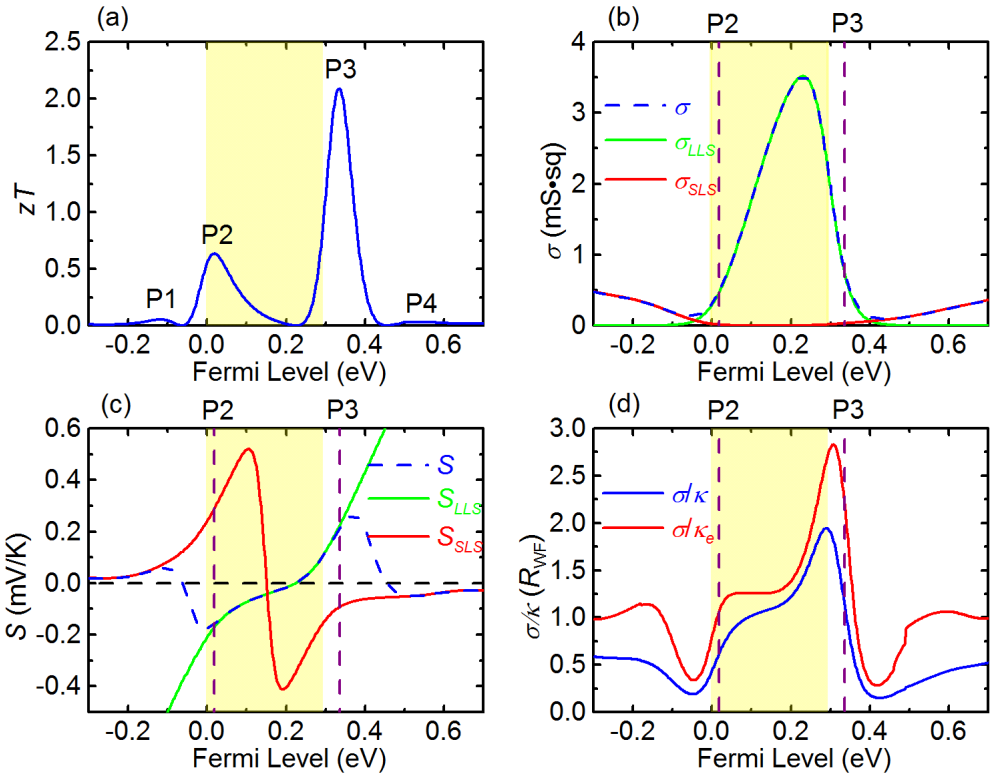

FIG. 2: **The room-temperature thermoelectric parameters of the** 8**QL** $\mathbf{Bi_2Se_3}$ **as functions of the Fermi level.** (**a**) The figure of merit. (**b**) The electrical sheet conductance σ and the LLS (SLS) conductance σ_{LLS} (σ_{SLS}). (**c**) The Seebeck coeffcient S and the LLS (SLS) Seebeck coeffcient S_{LLS} (S_{SLS}). (**d**) The ratio of σ to the (electronic) thermal sheet conductance κ (κ_e). The relaxation time of the LLSs and the SLSs are, respectively, set to be 230 fs and 1 fs. The vertical dashed lines in (**b**), (**c**), and (**d**) indicate the P2 and P3 energies.

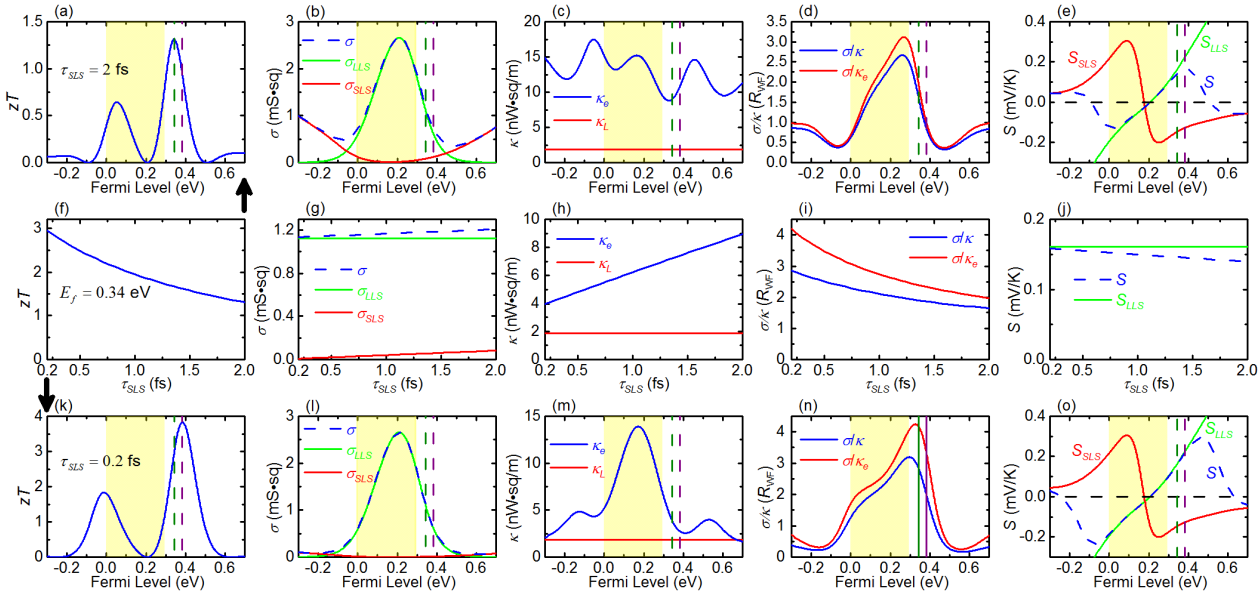

FIG. 3: **The thermoelectric parameters of the** 8**QL** Bi_2Se_3 **at temperature** $T = 600$ **K.** (**a-e**) The thermoelectric parameters as functions of the Fermi level for the SLS relaxation time being set at $\tau_{SLS} = 2$ fs and (**k-o**) those for $\tau_{SLS} = 0.2$ fs. In (**a-e**) and (**k-o**), the vertical green line and the vertical purple line indicate, respectively, the P3 energy for $\tau_{SLS} = 2$ fs and that for $\tau_{SLS} = 0.2$ fs. (**f-j**) The thermoelectric parameters as functions of SLS relaxation time when the Fermi level is set at 0.34 eV, the P3 energy for $\tau_{SLS} = 2$ fs.

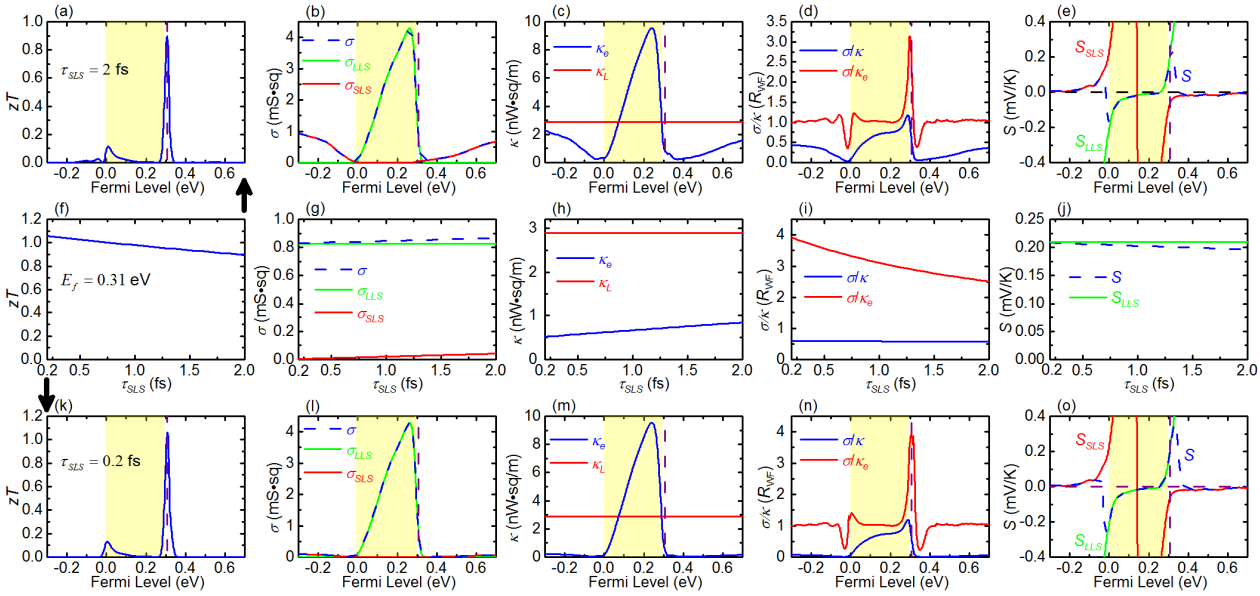

FIG. 4: **The thermoelectric parameters of the** 8**QL** Bi_2Se_3 **at temperature** $T = 100$ **K.** (**a-e**) The thermoelectric parameters as functions of the Fermi level for the SLS relaxation time being set at $\tau_{SLS} = 2$ fs and (**k-o**) those for $\tau_{SLS} = 0.2$ fs. (**f-j**) The thermoelectric parameters as functions of SLS relaxation time when the Fermi level is set at the P3 energy, 0.31 eV, which is denoted in (**a-e**) and (**k-o**) by the vertical purple lines.

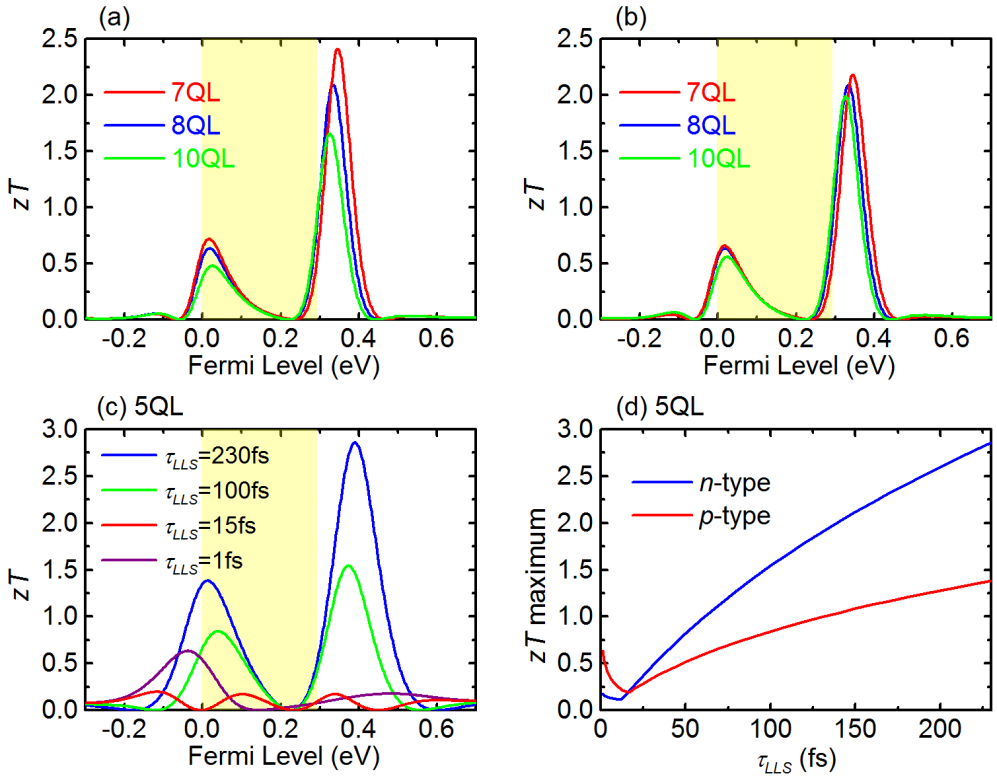

FIG. 5: **The thickness dependence of the figure of merit in the Bi_2Se_3 thin films.** (**a**) The room-temperature figure of merit as a function of Fermi level for the films of different thickness. (**b**) The same as (**a**) except that the lattice thermal conductance of all the films are set at the value the same as that of the 8QL film. (**c**) The figure of merit of the 5QL film at temperature $T = 600$ K as a function of the Fermi level. (**d**) The zT maximum of the 5QL film at temperature $T = 600$ K as a function of the LLS relaxation time for n-type (p-type) doping, i.e., for $E_f > 0.2$ eV ($E_f < 0.2$ eV). The relaxation time of the LLSs in (**a, b**) is set at 230 fs and that of the SLSs in (**a-d**) 1fs.

Supplementary Information of Enhanced Thermoelectric Performance in Thin Films of Three-Dimensional Topological Insulators

T. H. Wang and H. T. Jeng

Department of Physics, National Tsing Hua University,

101 Section 2 Kuang Fu Road, Hsinchu,Taiwan 30013,R.O.C.

arXiv:1608.00348v1 [cond-mat.mes-hall] 1 Aug 2016

Table of contents:

I. **Estimation of the LLS relaxation time**

II. **TE performance in the limit of large LLS relaxation time**

II. **Further Enhancement by shortening the SLS relaxation time at room temperature**

S1. ESTIMATION OF THE LLS RELAXATION TIME

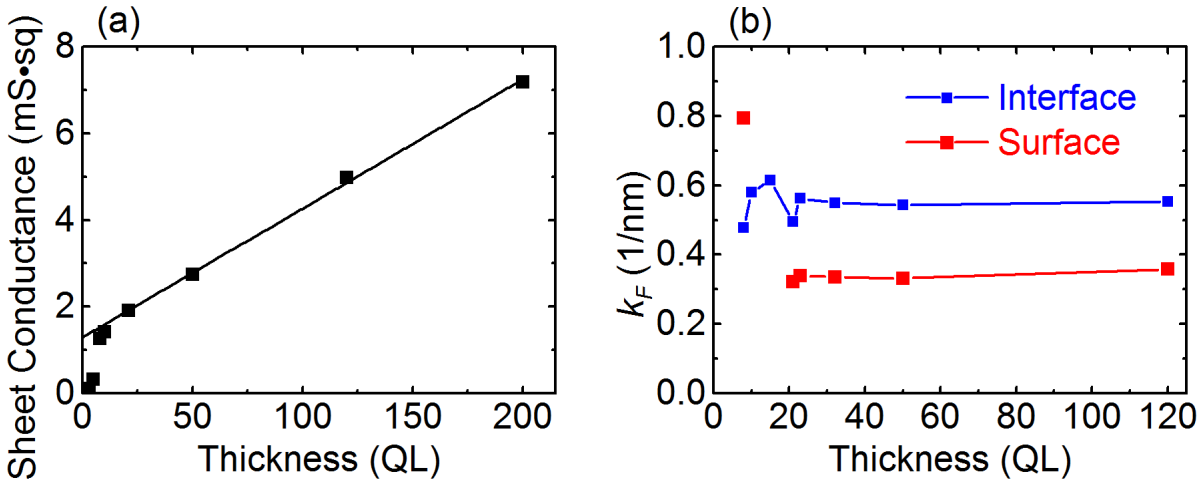

FIG. S1: **The room-temperature sheet conductance and Fermi wave number for the films of different thickness measured in ref. 1. (a)** The sheet conductance. The dots are the experimental data points and the straight line is a linear fit to the data points of thickness larger than 20 QLs. **(b)** The surface (interface) Fermi wave number obtained from the Fourier spectra of the Shubnikov-de Haas oscillations.

The relaxation time of the LLSs (i.e., the TSSs in the bulk gap) of the Bi_2Se_3 films can be estimated by comparing the measured sheet conductance in ref. 1 with our calculated results. Figure S1a shows the measured sheet conductance of the samples with different thickness at room temperature. As can be seen, the sheet conductance increases linearly with the film thickness for the samples of thickness $d \geq 8$ QLs. The linear dependence of the conductance on the film thickness implies that the carrier concentration and hence the Fermi energy of theses samples in the region away from the surface are nearly the same. The latter, according to the Mott criterion, should be near the CBE[2]. The intercept at zero thickness, $\sigma(0)$, should be be nearly equal to the sheet conductance of the LLSs. The conductance drops dramatically when the film thickness decreases from 8 QLs to 5 QLs indicating the dramatic decrease of the LLS relaxation time. This is an experimental evidence that the scattering between the TSSs on the opposite sides of the thin film becomes effective when the film thickness decreases from 8 QLs to 5 QLs. It is worth noting that the large-angle scattering between the TSSs on the same side is suppressed while that between

the TSSs on the opposite sides is enhanced because the spin polarizations of the TSSs at different sides circulate the circular energy contour oppositely. The linear dependence of the conductance on the film thickness also indicates that the LLS conductances and hence the surface (interface) Fermi energies of the samples whose thickness is not smaller than 8 QLs should be almost the same. The surface (interface) Fermi wave number k_F can be obtained from the Fourier transform of the Shubnikov-de Haas (SdH) oscillations reported in ref. 1. In general, there are two oscillation frequencies corresponding to the Fermi wave numbers at different sides of the Bi_2Se_3 film (i.e., the surface and the interface between the Bi_2Se_3 film and the substrate) as plotted in Fig. S1b. As can be seen, the SdH frequency corresponding to $k_F \sim 0.55$ (1/nm) always exists while the other one does not. Therefore, the former should be resulted from the interface while the latter the surface. The surface time-dependent downward band bending of the Bi_2Se_3 has been commonly observed. For example, it has been seen, when the Bi_2Se_3 surface is exposed to the carbon monoixide[3], the water vapor[4], the ambient environment[5] and even the residual gas in vacuum[6]. It can be the surface downward band bending effect so that the SdH oscillation of the surface TSS is not observed for the samples of thickness 10 QLs and 15 QLs[2], and the magnitude of the surface Fermi wave number of the 8QL samples is much larger than the samples of thickness larger than 20 QLs. When the surface Fermi level is higher than the CBE due to the surface downward band bending, the conductance contributed from the TSSs near the surface should be much smaller than that near the interface[2]. In the conductance measurement in ref. 1, the conductance contributed from the TSS near the surface should be negligible, otherwise the total conductance shown in Fig. S1a will not exhibit a linear dependence on the film thickness. Using the Fermi wave number $k_F = 0.55$ (1/nm), we get the Fermi level $E_f = 145$ meV. Comparing the LLS conductance $\sigma(0) = 1.29$ mS·sq, i.e. the intercept of the straight line in Fig. S1a, with our calculation of the LLS conductance σ_{LLS}, we conclude that the LLS relaxation time is about 230 fs.

S2. TE PERFORMANCE IN THE LIMIT OF LARGE LLS RELAXATION TIME

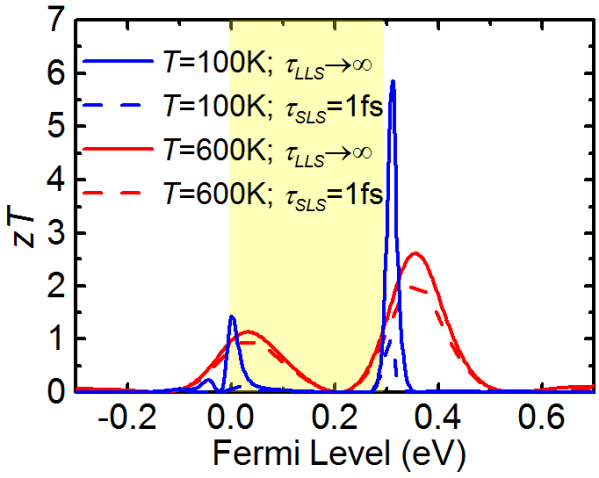

FIG. S2: **The figure of merit of the 8QL Bi_2Se_3 as a function of the Fermi level at temperatures $T = 100$ K (blue lines) and $T = 600$ K (red lines).** The ratio of the LLS to the SLS relaxation time τ_{LLS}/τ_{SLS} is set to be 230. The solid lines are the results in the limit of infinite LLS relaxation time and the dashed lines are for the case of $\tau_{SLS} = 1$ fs.

From Figs. 3a (3k) and 4a (4k) in the main text, we find the peak value of the figure of merit at low temperature ($T = 100$ K) is much smaller than that at high temperature ($T = 600$ K). However, thus far, we set the LLS relaxation time $\tau_{LLS} = 230$ fs, which, to some extent, is determined by the sample quality. The LLS relaxation time could be further extended by improving the surface quality (or more precisely, the sample quality in the region 3 QLs near the surface according to our calculation of the TSS wave functions). If the LLS relaxation time is so long that the electronic thermal conductance is much larger than the lattice thermal conductance, the peak value of the figure of merit at low temperature could be higher than that at high temperature. In the limit of infinite LLS relaxation time, the ratio σ/κ, Seebeck ceofficeint S, and hence the figure of merit zT do not correlate with τ_{LLS} or τ_{SLS} for a given relaxation time ratio $r_\tau \equiv \tau_{LLS}/\tau_{SLS}$. Figure S2 shows the resultant figure of merit, of which the r_τ is set to be 230. As can be seen, the maximum of the figure of merit at 100 K is more than twice larger than that at 600 K in the limit of infinite LLS relaxation time (Solid lines). As a comparison, the dashed lines shows the case of $\tau_{SLS} = 1$ fs, and the maximum of the figure of merit at 100 K is more than twice smaller than that

at 600 K.

S3. FURTHER ENHANCEMENT BY SHORTENING THE SLS RELAXATION TIME AT ROOM TEMPERATURE

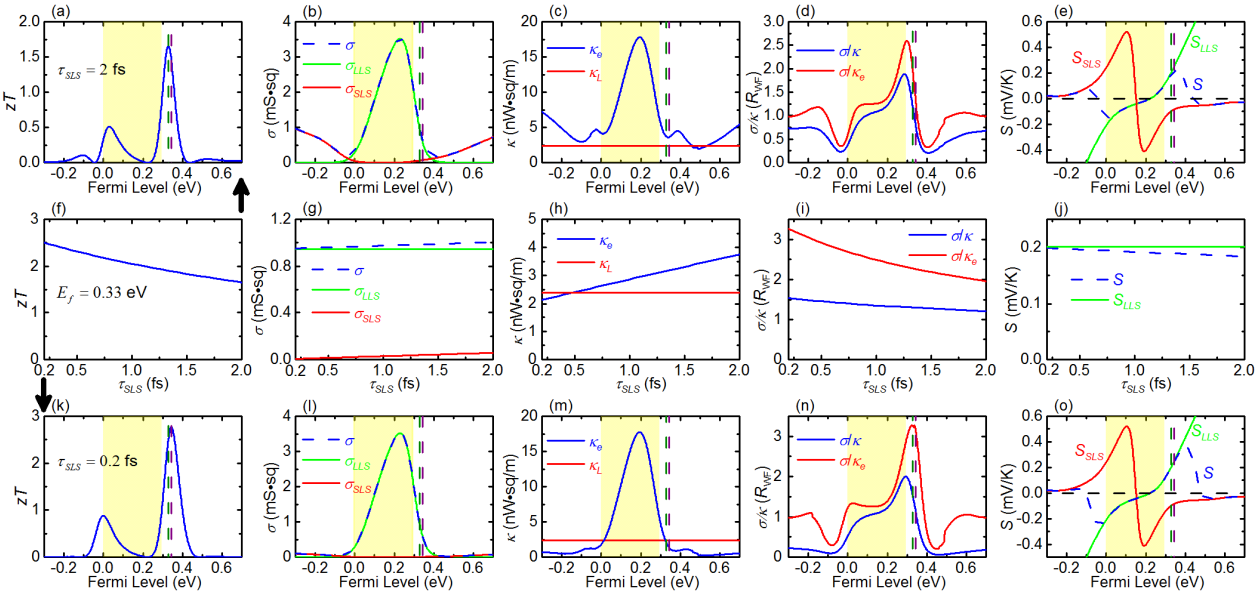

FIG. S3: **The thermoelectric parameters of the 8QL Bi_2Se_3 at temperature $T = 300$ K.** (**a-e**) The thermoelectric parameters as functions of the Fermi level for the SLS relaxation time being set at $\tau_{SLS} = 2$ fs and (**k-o**) those for $\tau_{SLS} = 0.2$ fs. In (**a-e**) and (**k-o**), the vertical green line and the vertical purple line indicate, respectively, the P3 energy for $\tau_{SLS} = 2$ fs and that for $\tau_{SLS} = 0.2$ fs. (**f-j**) The thermoelectric parameters as functions of SLS relaxation time when the Fermi level is set at 0.33 eV, the P3 energy for $\tau_{SLS} = 2$ fs.

[1] Taskin, A. A., Sasaki, S., Segawa, K. & Ando, Y. Manifestation of topological protection in transport properties of epitaxial Bi_2Se_3 thin films. *Phys. Rev. Lett.* **109**, 066803 (2012).

[2] Brahlek, M., Koirala, N., Bansal, N. & Oh, S. Transport properties of topological insulators: Band bending, bulk metal-to-insulator transition, and weak anti-localization. *Solid State Commun.* **215**, 54-62 (2015).

[3] Bianchi, M., Hatch, R. C., Mi, J. L., Iversen, B. B. & Hofmann, P. Simultaneous quantization of bulk conduction and valence states through adsorption of nonmagnetic impurities on Bi_2Se_3. *Phys. Rev. Lett.* **107**, 086802 (2011).

[4] Benia, H. M., Lin, C. T., Kern, K. & Ast, C. R. Reactive chemical doping of the Bi_2Se_3 topological insulator. *Phys. Rev. Lett.* **107**, 177602 (2011).

[5] Bianchi, M., Guan, D. D., Bao, S. N., Mi, J. L., Iversen, B. B., King, P. D. C. & Hofmann, P. Coexistence of the topological state and a two-dimensional electron gas on the surface of Bi_2Se_3. *Nat. Commun.* **1** (2010).

[6] King, P. D. C., Hatch, R. C., Bianchi, M., Ovsyannikov, R., Lupulescu, C., Landolt, G., Slomski, B., Dil, J. H., Guan, D., Mi, J. L., Rienks, E. D. L., Fink, J., Lindblad, A., Svensson, S., Bao, S., Balakrishnan, G., Iversen, B. B., Osterwalder, J., Eberhardt, W., Baumberger, F. & Hofmann, P. Large tunable Rashba spin splitting of a two-dimensional electron gas in Bi_2Se_3. *Phys. Rev. Lett.* **107**, 096802 (2011).